

Evaporation residue cross section in the $^{37}\text{Cl} + ^{68}\text{Zn}$ fusion reaction near the Coulomb barrier

Amit Chauhan¹, Rinku Prajapat¹, Gayatri Sarkar¹, Moumita Maiti^{1,*}, Rishabh Kumar¹, Malvika¹, Gonika², J. Gehlot², S. Nath², A. Parihari², and N. Madhavan²

¹*Department of Physics, Indian Institute of Technology Roorkee, Roorkee-247667, Uttarakhand, India*

²*Nuclear Physics Group, Inter-University Accelerator Centre, New Delhi-110067, India*



(Received 20 July 2020; accepted 12 November 2020; published 9 December 2020)

Background: The measured subbarrier fusion cross sections in heavy-ion reactions are found to be significantly large as compared with those expected from the one-dimensional barrier penetration model (1d-BPM). Although attempts have been made to comprehend the enhancement in terms of different intrinsic degrees of freedom of the colliding nuclei, a clear understanding of the same is yet to come.

Purpose: The objectives of this study is to understand the interplay of the channel coupling effect on fusion excitation function and explore the decay dynamics of the excited compound nucleus in the sub-and-near barrier region.

Method: Fusion excitation function has been measured at energies from 7% below to 38% above the Bass barrier using a recoil mass spectrometer. Furthermore, cross sections of the different evaporation residues, such as 98, 99, 100, and 101 u, have been extracted.

Results: The observed enhancement in the subbarrier fusion cross sections over the 1d-BPM predictions has been explained by considering the low-lying inelastic excitations among the interacting partners using CCFULL code and by the barrier modification using the dynamical cluster-decay model (DCM). The cross sections of individual residual mass fractions (98, 99, 100, and 101 u) have been compared with the Hauser-Feshbach model.

Conclusion: Coupled-channel calculations and DCM have successfully explained the total fusion cross sections data. The measured total fusion cross section σ_{fus} was found to be approximately equal to the sum of various residual mass fractions ($\Sigma\sigma_{\text{ER}}$) at energies above the Bass barrier. One-dimensional barrier height and radius parameters extracted from the measured data are in good agreement with the Bass model and DCM parameters.

DOI: [10.1103/PhysRevC.102.064606](https://doi.org/10.1103/PhysRevC.102.064606)

I. INTRODUCTION

Bohr's independence hypothesis predicts the complete equilibration and loss of memory of the entrance channel in the fused compound nucleus formed in an interaction between two colliding nuclei at near-barrier energies. Depending on the available kinetic energy, the fusion of two atomic nuclei broadly occurs either by passing over or quantum tunneling [1] through the Coulomb barrier. The subbarrier fusion of light nuclei is used to understand stellar nucleosynthesis processes [2], and complete fusion of heavy-mass nuclei leading to the synthesis of heavy and superheavy elements [3]. Fusion reactions have also been extensively studied in the past few decades to understand the interplay of nuclear structure and reactions at energies near the Coulomb barrier [4–7].

The measured subbarrier fusion cross sections in heavy-ion reactions were found to be significantly large as compared with those expected from the one-dimensional barrier penetration model (1d-BPM), where the potential is expressed only as a function of the distance of separation between the centres of colliding nuclei [8–23]. The observed enhancement in the subbarrier fusion cross sections could be understood in terms

of different intrinsic degrees of freedom of colliding partners, such as couplings of inelastic excitations [8–10,12], deformations [13–15], vibrational modes [16,17], nucleon transfer [18–22], etc. Besides the relative motion of colliding partners, these intrinsic degrees of freedom are essential and subtle components of the interaction potential that impact the fusion phenomenon at subbarrier energies. The nuclear deformation and couplings of inelastic channels such as rotational or vibrational couplings distribute and split the one-dimensional barrier into a distribution of barriers [1,5,7]. The distribution of barriers modifies the fusion probability, enhancing subbarrier fusion cross sections over the predictions from 1d-BPM.

In the literature, enhancement in subbarrier fusion cross sections of ^{12}C , ^{16}O , ^{28}Si , and ^{35}Cl with ^{92}Zr was demonstrated, and the barrier distributions were extracted. The enhancement in cross sections below the one-dimensional barrier was attributed to the inelastic couplings between projectiles and target; however, fusion cross sections at low energies were better reproduced by also considering two-neutron pickup channels in ^{28}Si , $^{35}\text{Cl} + ^{92}\text{Zr}$ reactions [23]. Furthermore, the role of coupling of collective states along with transfer channels in subbarrier fusion cross-section enhancement has been extensively demonstrated in ^{28}Si -induced reactions on $^{90,92,94,96}\text{Zr}$ [10–12]. It was observed that $^{28}\text{Si} + ^{94}\text{Zr}$ has a significantly large subbarrier fusion cross

*Corresponding author: moumita.maiti@ph.iitr.ac.in

section as compared with $^{28}\text{Si} + ^{90}\text{Zr}$, indicating the role of multinucleon transfer with positive Q value in the $^{28}\text{Si} + ^{94}\text{Zr}$ system. Later, it was confirmed by the same group that $^{28}\text{Si} + ^{94}\text{Zr}$ has a large transfer probability (up to four neutrons with positive Q value) compared with the $^{28}\text{Si} + ^{90}\text{Zr}$ reaction; it helped to establish a correlation between the transfer and fusion phenomenon [11].

Likewise, the role of nuclear deformation on subbarrier fusion enhancement has extensively been studied for the ^{16}O -induced reaction on various isotopes of Sm, having a spherical or deformed structure [15]. A similar effect has been explored due to deformation in $^{37}\text{Cl} + ^{70,72,73,74,76}\text{Ge}$ systems [13], where prolate shape of $^{74,76}\text{Ge}$ isotopes were assumed; however, this data could not discriminate the structural effect between spherical (vibrational) ^{37}Cl and oblate-deformed ^{37}Cl . The experimental data were in good agreement with CCFCUS predictions by considering ^{37}Cl and ^{64}Ni as static oblate deformed and other Ni isotopes as spherical vibrators in $^{37}\text{Cl} + ^{58,60,62,64}\text{Ni}$ reactions [16]. Furthermore, it was emphasized in the literature that subbarrier fusion of $^{35,37}\text{Cl}$ [22] was more enhanced by the inelastic coupling effect compared with the subbarrier fusion of $^{34,36}\text{S}$ with the same nickel targets. Analysis of the excitation functions of Cl + Ni and S + Ni in terms of reduced energy and cross sections indicated the transfer effect with positive Q value, probably one- or two-proton-stripping channels, in $^{35,37}\text{Cl} + ^{64}\text{Ni}$ reactions. Similarly, inclusion of inelastic excitations and transfer channels explained subbarrier fusion enhancement for $^{37}\text{Cl} + ^{98,100}\text{Mo}$ systems while it failed to reproduce the $^{37}\text{Cl} + ^{93}\text{Nb}$ results [18].

For the estimation of the fusion cross section using the barrier passing model, the energy-independent Woods-Saxon (WS) form of nuclear potential is extensively used:

$$V_N(r) = -\frac{V_0}{1 + e^{(r-R)/a}}, \quad (1)$$

where $R = r_0(A_p^{1/3} + A_t^{1/3})$, A_p , A_t are the mass numbers of projectile and target, respectively; V_0 , r_0 , and a are the depth, radius parameter, and diffuseness parameter, respectively. The combined effect of nuclear, Coulomb, and centrifugal potential results in the fusion barrier. Hagino *et al.* [24] pointed out the use of a range of diffuseness parameter ($a = 0.65$ to 1.3 fm) to explain the fusion cross section. It may be ascribed to the large diffuseness leading to the small barrier position and smaller barrier curvature, expanding the tunneling region. Some of the experiments chose a range of a values (between 0.65 to 1.5 fm) to reproduce the fusion cross sections but failed to reproduce the fusion excitation functions around the Coulomb barrier [8,25]. It possibly indicates that the WS potential's simple form may not be appropriate for an actual nuclear potential in the Coulomb barrier vicinity. Besides this, other nuclear processes such as suppression in fusion cross section due to the breakup of projectile [26,27], complete-incomplete fusion (CF-ICF) [26,28–31], and pre-equilibrium (PEQ) reactions emerge in the dynamics of light-heavy-ion-induced reactions on medium- or heavy-mass nuclei above Coulomb-barrier energies [32–36].

It is clear from the existing reports that the fusion phenomenon is still less understood, particularly in the subbarrier-energy region, due to different structural properties, the unknown nature of nuclear potential around the Coulomb barrier, and transfer channels of interacting partners. Thus, more experimental data sets are required to understand the interplay of the nuclear structure effect on subbarrier fusion phenomena. This article presents a study of the fusion excitation function of $^{37}\text{Cl} + ^{68}\text{Zn}$ system over a wide energy range, 61.4 – 90.0 MeV. A ^{68}Zn target has a relatively higher N/Z ratio but a similar deformation parameter compared with those reported so far in the same mass range. The study mainly aims to explore the channel-coupling effect on fusion excitation functions in the sub- and near-barrier regions and to understand the decay mechanism of the excited compound nucleus $^{105}\text{Ag}^*$, which is formed through the fusion of ^{37}Cl in ^{68}Zn , using a nonstatistical approach. Furthermore, the chosen reaction could help in optimizing reaction parameters at the above-barrier region for cumulative production of $^{100,101}\text{Pd}$, which will decay to $^{100,101m}\text{Rh}$ radionuclides that are medically relevant radionuclides [37,38].

The experimental work is presented in Sec. II. A description of the data analysis is provided in Sec. III. Section IV sheds light on the results, and, finally, Sec. V concludes the article.

II. EXPERIMENTAL DETAILS

The experiment was carried out at the 15UD Pelletron accelerator facility of Inter-University Accelerator Center (IUAC), New Delhi, India, using the recoil mass spectrometer, Heavy Ion Reaction Analyzer (HIRA) [39]. A thin ^{68}Zn target, having a thickness of $370 \mu\text{g}/\text{cm}^2$, was prepared on a $30 \mu\text{g}/\text{cm}^2$ carbon backing. The purity and thickness of the prepared ^{68}Zn target was analyzed by using the Rutherford backscattering setup of IUAC. A pulsed beam of ^{37}Cl with $2 \mu\text{s}$ separation was used to bombard the ^{68}Zn target. The fusion excitation function was measured from the $^{37}\text{Cl} + ^{68}\text{Zn}$ reaction within the energy range of 94.8 – 138.9 MeV in the laboratory frame of reference ($E_{\text{c.m.}} = 61.4$ – 90 MeV) in steps of 2 and 5 MeV, near and above the one-dimensional (uncoupled) Coulomb barrier, respectively, covering $\approx 7\%$ down to $\approx 38\%$ above the Coulomb barrier. The incident projectile energies were corrected considering the energy loss in the half thickness of ^{68}Zn target and carbon backing, which was made to face the beam.

HIRA rejects primary beam-like particles at 0° , with respect to the beam direction, using various electromagnetic components and transports recoiling evaporation residues (ERs) from the target chamber to the focal plane, dispersing them according to their m/q ratio. In the present experiment, the spectrometer was kept at 0° in regard to the beam direction with a solid angle acceptance set at five mSr. Two silicon surface barrier detectors (SSBD) with 1 mm diameter aperture were installed inside the sliding-seal target chamber at $\pm 15.5^\circ$ about the incident-beam direction to monitor the beam and normalize the yield of ERs required to estimate the cross sections. A carbon foil of $\approx 30 \mu\text{g}/\text{cm}^2$ thickness was placed 10 cm downstream from the target to reset the charge state of

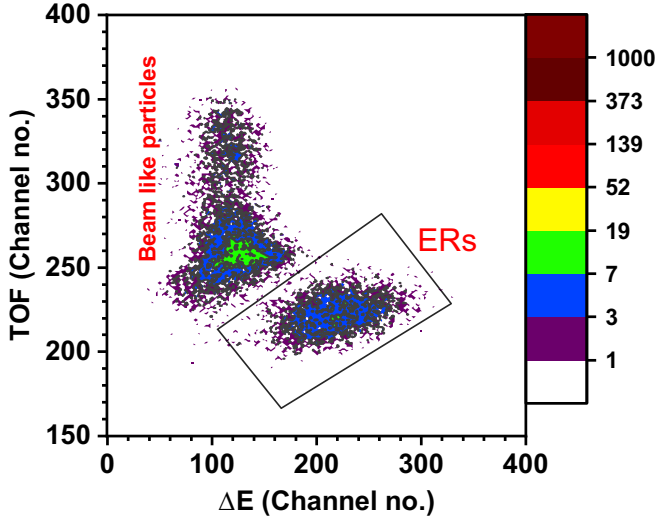


FIG. 1. Two-dimensional spectrum showing the TOF (y axis) vs energy loss (x axis) of particles in MWPC for $^{37}\text{Cl} + ^{68}\text{Zn}$ for the fusion-evaporation reaction at $E_{c.m.} = 86.7$ MeV. The area enclosed by black solid lines represent the group of ERs which are well separated from beam-like particles.

ERs back to statistical distribution after possible deviation due to multi-Auger processes.

A two-dimensional position-sensitive multiwire proportional counter (MWPC) with an active area of 150×50 mm² was used at the HIRA's focal plane to detect recoiling ERs. The timing information was obtained through the time-to-amplitude converter (TAC) with the arrival of particles at the MWPC as the start signal and a delayed RF signal as the stop signal. A setup was used to achieve the coincidence between RF and MWPC anode signal before using it as the TAC stop. It helped in reducing unnecessary RF pulses going to the TAC. The time-of-flight (TOF) information helped the separation of multiple scattered beam-like particles from ERs at the focal plane of the HIRA spectrometer. The yield of ERs was extracted by using the two-dimensional spectrum of energy loss (ΔE) (from the cathode signal of MWPC) vs TOF by identifying the ER group from large MWPC signals. Because the system ($^{37}\text{Cl} + ^{68}\text{Zn}$) is relatively symmetric (mass asymmetry = $\frac{A_p - A_t}{A_p + A_t} = 0.3$), expected beam-like particles are comparable to ERs at the focal plane of HIRA, as shown in Fig. 1. HIRA's field was scanned to find the most probable charge state, mass, and energy of ERs in $^{37}\text{Cl} + ^{68}\text{Zn}$ reaction at 133.9 MeV (E_{lab}); the best setting was obtained by looking for maximum transmission efficiency and clear separation of ERs from the beam-like particles at each incident energy.

III. DATA ANALYSIS

In this experiment, since fission is negligible for the $^{37}\text{Cl} + ^{68}\text{Zn}$ reaction, the measured total ER cross section has been considered as the fusion cross section. The total ER cross section has been calculated from the following:

$$\sigma_{\text{fus}} = \frac{Y_{\text{ER}}}{Y_{\text{norm}}} \left(\frac{d\sigma}{d\Omega} \right)_{\text{Ruth}} \Omega_{\text{norm}} \frac{1}{\epsilon_{\text{HIRA}}}, \quad (2)$$

where σ_{fus} is the fusion cross section (mb), Y_{ER} is the yield of ERs at the focal plane of HIRA detected by the MWPC, and $Y_{\text{norm}} = \sqrt{M_L M_R}$ (M_L , M_R are the left and right monitor detector counts) is the geometric mean of monitor yields. $(\frac{d\sigma}{d\Omega})_{\text{Ruth}}$ is the differential Rutherford scattering cross section (mb/Sr) in the laboratory frame of reference, Ω_{norm} (Sr) is the solid angle subtended by each monitor detector, and ϵ_{HIRA} is the average transmission efficiency of HIRA. ϵ_{HIRA} , a crucial parameter to measure the absolute cross section of ERs, is defined as

$$\epsilon_{\text{HIRA}} = \frac{\text{number of ERs detected by the MWPC}}{\text{number of ERs produced}}. \quad (3)$$

It depends on several factors, such as entrance-channel mass asymmetry, projectile energy, target thickness, solid angle acceptance of HIRA, evaporation channel, and size of the focal plane detector, [40]; hence, ϵ_{HIRA} is different for each incident energy. During the experiment, HIRA's transmission efficiency is normally measured by γ detection in both coincidence and singles mode [10]. In the present analysis, HIRA's transmission efficiency is estimated by semimicroscopic Monte Carlo code TERS [41], which can find the transmission efficiency within an accuracy of $\approx 10\%$ [10,40]. Moreover, the possibility of the relative production of different ERs has been estimated by using the statistical model code PACE4 [42] within the studied energy range for the $^{37}\text{Cl} + ^{68}\text{Zn}$ system, and HIRA was set for the most dominant ER channel. At each incident energy, we estimated the ER transmission efficiency through HIRA for each possible dominant ER channel by using the TERS code. The weighted average of HIRA efficiencies has been taken for possible evaporation channels for the estimation of the average transmission efficiency of HIRA (ϵ_{HIRA}) at each E_{lab} . The relative production of different ERs has been taken from the PACE4 code. The estimated range of ϵ_{HIRA} for the present system is 1.0–7.0%. Finally, with the help of an estimated ϵ_{HIRA} , the ER cross section has been calculated using Eq. (2). A detailed procedure for estimating HIRA's transmission efficiency using the TERS code can be found in Ref. [43].

IV. RESULTS AND DISCUSSION

A. Analysis of fusion cross section

The measured fusion cross sections of $^{37}\text{Cl} + ^{68}\text{Zn}$ reaction are presented in Table I. The uncertainty assigned to the measured cross sections accounts for the statistical error in ER counts, monitor yields, solid angle subtended by monitor detectors, and error in determining HIRA's transmission efficiency. Coupled channels (CC) calculations have been performed to analyze the measured data using the CCFULL code [44]. It can estimate the total fusion cross section and the average angular momentum by considering inelastic channel couplings in the projectile and target nuclei. The prediction of fusion cross section in the absence of channel couplings and the choice of potential as a function of only the distance of separation (r) is known as the one-dimensional barrier penetration model (1d-BPM). The code can handle calculations for those projectile-target combinations whose $Z_p + Z_t$ is larger than around 12 and the product of their charge, $Z_p Z_t$, is less

TABLE I. Measured $\sigma_{\text{fus}}^{\text{expt}}$ for the reaction $^{37}\text{Cl} + ^{68}\text{Zn}$, and the calculated complete fusion cross sections $\sigma_{\text{fus}}^{\text{DCM}}$ corresponding to the optimized values of ΔR , T , and ℓ_{max} .

Energy ($E_{\text{c.m.}}$) (MeV)	T (MeV)	ΔR (fm)	ℓ_{max} (\hbar)	$\sigma_{\text{fus}}^{\text{DCM}}$ (mb)	$\sigma_{\text{fus}}^{\text{expt.}}$ (mb)
61.4	0.23	0.84	63	0.10	0.10 ± 0.02
62.7	0.23	0.95	63	0.89	0.79 ± 0.14
64.0	0.23	1.05	63	3.12	3.96 ± 0.66
67.2	0.24	1.30	63	45.2	47.0 ± 7.6
70.5	0.25	1.44	63	163.0	166.1 ± 26.0
73.7	0.26	1.51	63	224.0	223.6 ± 35.2
77.0	0.26	1.54	63	315.0	313.3 ± 48.6
79.9	0.27	1.61	63	414.0	416.4 ± 66.4
83.5	0.27	1.61	63	453.0	447.9 ± 70.2
86.7	0.28	1.63	63	583.0	584.7 ± 93.7
90.0	0.29	1.67	63	608.0	605.4 ± 94.7

than around 1800. The ion-ion potential is a critical component of CC calculations, and, so far, various forms of nuclear potential have been simulated in the literature to justify the fusion data. In the present analysis, the Woods-Saxon ion-ion potential with Akyüz-Winther (AW) parametrization with $V_0 = 66$ MeV, $r_0 = 1.08$ fm, and $a = 0.92$ fm, has been implemented. These values were chosen to fit the above-barrier data and to produce equivalent Coulomb barrier parameters. Lines represent the predicted fusion cross sections from the CCFULL in Figs. 2(a) and 2(b).

The measured fusion cross sections of $^{37}\text{Cl} + ^{68}\text{Zn}$ reaction have been compared with the theoretical estimations obtained from CCFULL, as shown in Fig. 2(a). The predicted subbarrier fusion cross sections from the 1d-BPM are significantly low compared with the measured data. The observed difference between the measured fusion cross sections and 1d-BPM

TABLE II. Excitation energies (E^*), spin-parity (J^π), transition (E_λ), and deformation parameters (β_λ) [8,9] of ^{37}Cl and ^{68}Zn used in the coupled-channels calculations.

Nucleus	E^* (MeV)	J^π	E_λ	β_λ
^{37}Cl	1.73	vib. $(1/2)^+$	2	0.14
	3.09	vib. $(5/2)^+$	2	0.24
^{68}Zn	1.08	2^+	2	0.21
	2.75	3^-	3	0.23

prediction can be understood by including the low-lying inelastic channel couplings in the projectile and target. The low-lying inelastic states of ^{37}Cl and ^{68}Zn with corresponding excitation energy, deformation parameter, and spectroscopic properties are listed in Table II. Coupled channels calculations have been performed considering ^{37}Cl (p) and ^{68}Zn (t) as vibrators. The inclusion of coupling between $(5/2)^+$ vibrational state of ^{37}Cl with one-phonon enhanced the fusion cross sections as compared with $(1/2)^+$ state with one phonon, as seen in Fig. 2(a). The observed enhancement may be due to the large deformation strength of $(5/2)^+$ state as compared with the $(1/2)^+$ state of ^{37}Cl . The 2^+ state of ^{68}Zn also enhances the cross section almost by the same amount. This may be due to comparable deformation strength of $p(5/2)^+$, $t(2^+)$ and $t(3^-)$ states. Although CC calculations enhanced the cross sections after the inclusion of individual channel couplings, it failed to reproduce the measured data. Therefore, couplings in $p-t$ together and mutual excitations in $t(2^+, 3^-)$ states were incorporated in the calculations. After considering the mutual excitations in $(2^+, 3^-)$ states with single-phonon coupling, i.e., $2^+ \otimes 3^-$, CC calculation provides a significant enhancement, particularly at the subbarrier region. However, it still underpredicts the measured data below the Coulomb

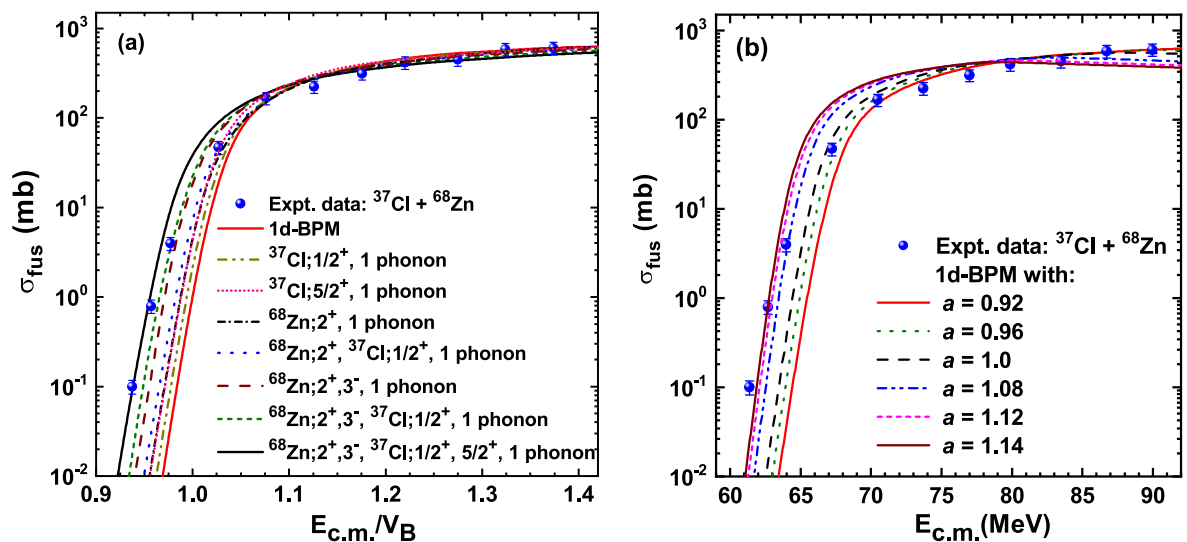


FIG. 2. (a) Measured fusion excitation function of $^{37}\text{Cl} + ^{68}\text{Zn}$ reaction has been compared with 1d-BPM and those obtained after considering different modes of inelastic couplings in projectile and target in CCFULL. (b) Measured fusion excitation function has been compared with those predicted from the 1d-BPM with different diffuseness parameter.

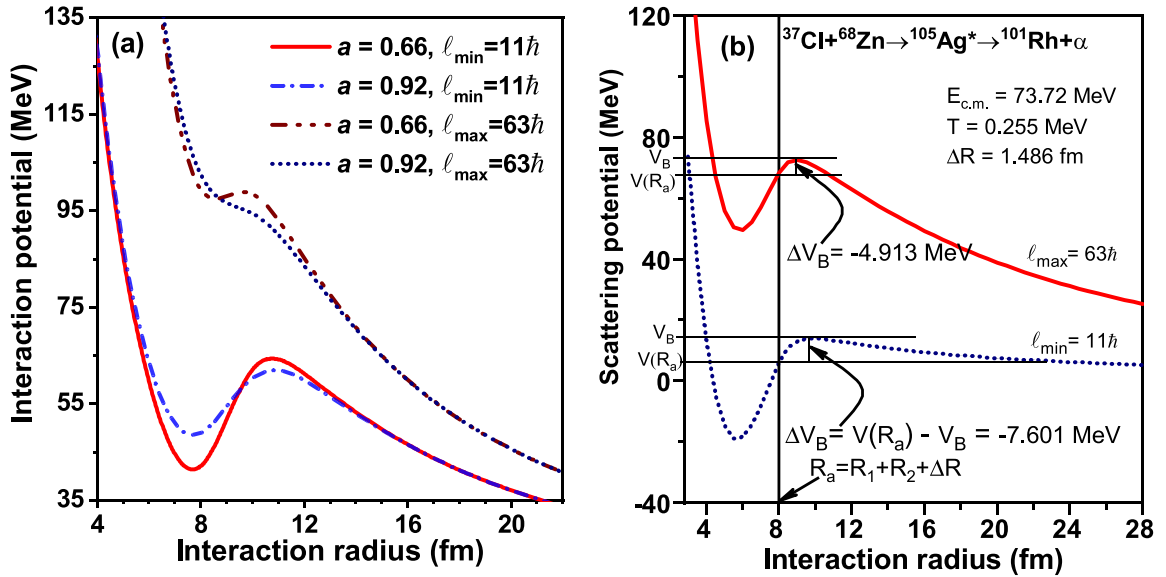


FIG. 3. (a) Effect of diffuseness parameter a on total interaction potential energy ($V_{\text{total}} = V_{\text{Coulomb}} + V_{\text{Nuclear}} + V_{\text{Centrifugal}}$) pocket at $\ell_{\min} = 11\hbar$ and $\ell_{\max} = 63\hbar$ for $^{37}\text{Cl} + ^{68}\text{Zn}$ reaction at $E_{c.m.} = 73.7$ MeV. (b) The scattering potential $V(R, \ell)$ used in the DCM as a function of interaction radius for the compound system $^{105}\text{Ag}^*$ formed in the $^{37}\text{Cl} + ^{68}\text{Zn}$ reaction at $E_{c.m.} = 73.7$ MeV at two different angular momenta, ℓ_{\min} and ℓ_{\max} .

barrier, reproduces a couple of data points near the barrier, and slightly overpredicts them above the barrier. The combined coupling effects of the projectile, $p(1/2)^+$, with single phonon and target, $t(2^+ \otimes 3^-)$, slightly overestimated the experimental data at above barrier while they were very close to the measured data in below-barrier region. Furthermore, a combination of $t : (2^+ \otimes 3^-)$ and $p : (1/2)^+ \otimes (5/2)^+$ states coupling reproduce the measured sub- and above-barrier fusion cross sections except $E_{c.m.} = 73.7$ MeV.

The diffuseness parameter a in the Woods-Saxon potential is a crucial factor that defines the nuclear potential in the tail region of the Coulomb barrier. The a parameter is correlated to the barrier position and barrier curvature that influence the fusion cross sections below and above barrier energies. Measured cross section data have been compared with the 1d-BPM varying a within 0.92–1.14 fm, as shown in Fig. 2(b), to understand its effect on fusion. It can be observed that 1d-BPM with $a = 0.92$ could not reproduce the measured fusion cross sections in the below-barrier region. In contrast, it reproduces them mostly in the above-barrier region, except for a few. By increasing the diffuseness parameter, predicted fusion cross sections increase below ≈ 80 MeV beyond which they decrease; hence, 1d-BPM calculations with $a = 1.14$ fm reproduce the measured data at below-barrier energies while it overestimates those until 80 MeV and underestimates beyond it. The higher value of the diffuseness parameter leads to a smaller barrier height, shallower potential pocket, and small barrier curvature that enhances the tunneling region for a fixed ℓ value. However, barrier width decreases promptly for the higher angular momenta, as depicted in Fig. 3(a). Hence, a large tunneling width enhances the fusion cross sections at energies around the Coulomb barrier. The impact of diffuseness parameter on fusion cross sections is also available in the literature [6–8].

B. Contribution from mass fractions

The two-dimensional spectra of ERs, dispersed in the focal plane according to energy loss of ERs in the MWPC versus their m/q ratio, were recorded at each energy; a typical spectrum of such ER distribution is shown in Fig. 4(a) at $E_{c.m.} = 86.7$ MeV. The one-dimensional mass spectrum of ERs obtained by suitably projecting the ER-gated spectrum between energy loss ΔE and MWPC position (X) is also presented in Fig. 4(b). Cross sections of various mass fractions, such as mass 98 u, which is the sum of all 98 u residues (^{98}Ru and ^{98}Rh), similarly, mass fractions 99 u (^{99}Rh and ^{99}Pd), 100 u (^{100}Rh , ^{100}Pd , and ^{100}Ag), and 101 u (^{101}Pd and ^{101}Ag) have been measured from the gated data using Eq. (2) with $E_{c.m.} = 67.2$ – 90.0 MeV, shown in Figs. 5 and 6 and compared with the statistical model calculation of PACE4.

PACE4 [42], based on the Hauser-Feshbach (HF) formalism of compound reactions, is using the Monte Carlo procedure to determine the decay sequence of an excited nucleus. The code incorporates the angular-momentum projections at each stage of the deexcitation to predict the angular-momentum distribution of emitted particles. The fusion cross-section is estimated using the Bass model [45]. The transmission coefficients of evaporated light particles, such as n , p , α , etc., are determined from the optical model, whose parameters are taken from Ref. [46]. The level-density parameter a' used in this model is defined as $a' = A/K$, where A is the mass number of the compound nucleus, and K is a free parameter known as the level-density parameter constant. In the present analysis, we have used $K = 9$ and 11. More description of PACE4 can be found in Refs. [30,33].

Figures 5(a) and 5(b) show a comparison between measured and theoretical cross sections of masses 98 u and 99 u along with individual residues of mass 98 u (^{98}Ru and ^{98}Rh)

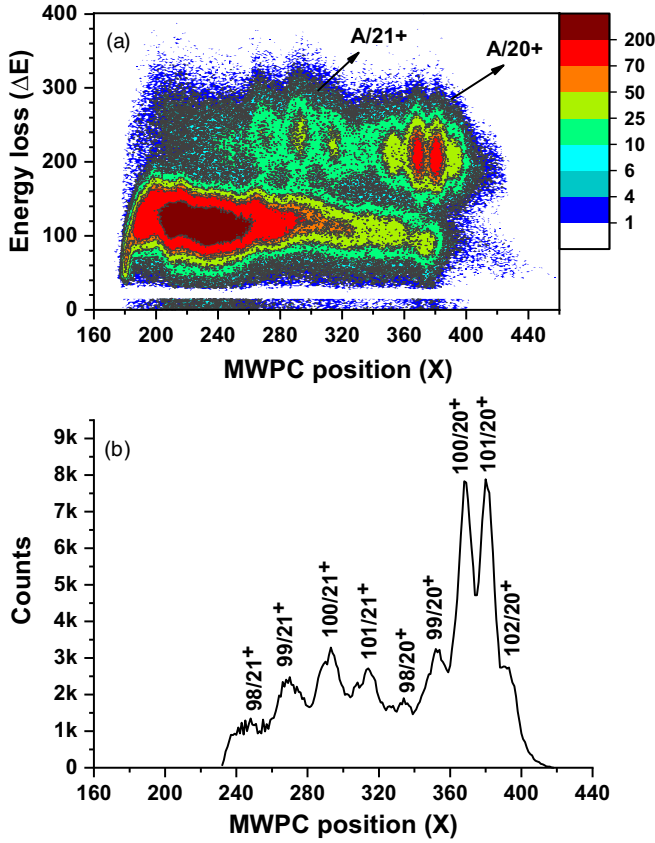


FIG. 4. (a) Two-dimensional mass spectrum showing the correlation between energy loss ΔE of the particles against position in MWPC (X). Two patches of evaporation residues are visible according to their m/q values. (b) Mass spectrum obtained by projecting the two-dimensional spectrum from panel (a) for $^{37}\text{Cl} + ^{68}\text{Zn}$ at $E_{c.m.} = 86.7$ MeV.

and 99 u (^{99}Rh and ^{99}Pd) obtained from PACE4 in order to see their plausible contribution. The experimental cross sections of mass 98 u are well reproduced beyond ≈ 82 MeV by the estimations with $K = 11$ while it slightly overpredicts them below 82 MeV. The experimental data of mass 99 u are nearly ten times enhanced than theoretical estimates throughout the energy range.

Figures 5(c) and 5(d) compare the measured excitation functions of masses 100 and 101 u with PACE4 and also show the contributions from individual residues of mass 100 u (^{100}Rh , ^{100}Pd , and ^{100}Ag) and 101 u (^{101}Pd and ^{101}Ag) estimated from PACE4 to understand their theoretical contribution. The measured excitation function of mass 100 u is underpredicted by PACE4 ($K = 9, 11$) below 80 MeV while overpredicted beyond 85 MeV; in between it comes to the proximity of PACE4. PACE4 values with $K = 9$ grossly agree with the measured cross sections of mass 101 u at two lower- and two higher-energy points only. Thus, it concludes that the Hauser-Feshbach model is unable to reproduce the cross sections of individual residual mass fractions (99, 100, and 101 u), except for the mass 98 u, using the chosen set of parameters.

Figure 6 depicts measured fusion cross sections σ_{fus} , sum of cross sections of all the residues having masses 97 u, 98 u,

99 u, 100 u, and 101 u ($\Sigma\sigma_{\text{ER}}$), and cross sections of individual residues of mass 97 u (^{97}Ru and ^{97}Rh), 98 u (^{98}Ru and ^{98}Rh), 99 u (^{99}Rh and ^{99}Pd), 100 u (^{100}Rh , ^{100}Pd , and ^{100}Ag), and 101 u (^{101}Pd and ^{101}Ag). It can be observed that the measured σ_{fus} and $\Sigma\sigma_{\text{ER}}$ are nearly equal above the barrier, which ensures the reliability of the measured data. The theoretical cross section of ERs of mass 99 u, predominantly populating via the αxn and pxn channels, is less in the above-barrier region, especially for $E_{c.m.} \approx 73\text{--}84$ MeV, HIRA efficiencies for the αxn and pxn channels are less as compared with xn channels. Hence, ϵ_{HIRA} , which is the weighted average of such evaporation channel efficiencies, also gets reduced in such cases, and that directly enhances the measured cross section for the individual mass fraction. Therefore, measured cross sections obtained from the sum of ERs are slightly greater than the measured fusion cross sections in the 73–84 MeV region.

C. Analysis of fusion cross section using the dynamical cluster-decay model

The dynamical cluster-decay model (DCM) [47,48] of Gupta and collaborators, is based on the quantum-mechanical fragmentation theory (QMFT) and considers the collective clusterization approach in which ERs, intermediate-mass fragments (IMFs), heavier-mass fragments (HMFs), and fission fragments (FFs) are considered on equal footing. It provides a nonstatistical description of decay channels and imparts relevant structural aspects of a deexciting nucleus that are missing in other statistical models [49]. QMFT works in terms of the collective coordinates of mass and charge asymmetry ($\eta_A = \frac{A_1 - A_2}{A_1 + A_2}$, $\eta_Z = \frac{Z_1 - Z_2}{Z_1 + Z_2}$), the relative separation R which is related to the quadrupole deformations β_{2i} and orientations θ_i ($i = 1, 2$) of daughter (A_1, Z_1) and cluster (A_2, Z_2) nuclei [50]. Furthermore, a detailed description of methodology of DCM can be seen in Ref. [51].

The neck length parameter ΔR , which is the length between two deformed, oriented nuclei, and the only adjustable DCM parameter, is strongly dependent on temperature T and ℓ_{max} . As a result, R_a , which decides the entry point of barrier penetration and the fragment preformation, is also T dependent. The $\Delta R(T)$ for the best fit to the data allows us to define the effective barrier-lowering parameter $\Delta V_B(\ell)$ as a difference between the actually used barrier $V(R_a, \ell)$ and top of the barrier $V_B(\ell)$ for each ℓ , i.e., $\Delta V_B(\ell) = V(R_a, \ell) - V_B(\ell)$. Since ΔV_B is defined as a negative quantity, the actually used barrier is effectively lowered, as shown in Fig. 3(b) for both ℓ_{min} and ℓ_{max} . The deexcitation of $^{105}\text{Ag}^*$, formed in the $^{37}\text{Cl} + ^{68}\text{Zn}$ reaction, has been studied using DCM in the experimental energy range $E_{c.m.} = 61.4\text{--}90.0$ MeV. The contributions of IMFs and FFs are minimal compared with ERs for the deexcitation of $^{105}\text{Ag}^*$. Thus, an attempt has been made to analyze ERs having contributions from neutron and charged particle fragments ($1n, 2n, ^3\text{H}, ^4\text{He}$) using DCM for the sticking limit of moment of inertia (I_s), β_2 deformations and θ_i^{opt} , optimum orientation of decaying fragments. However, different ΔR values have been chosen to explain the experimental data. The β_2 values are taken from the theoretical estimates of Moller and Nix [52], while θ_i^{opt} ($\theta_1 = 0^\circ, 90^\circ$; $\theta_2 = 90^\circ, 180^\circ$) are uniquely fixed based on the β_2 deformations for the

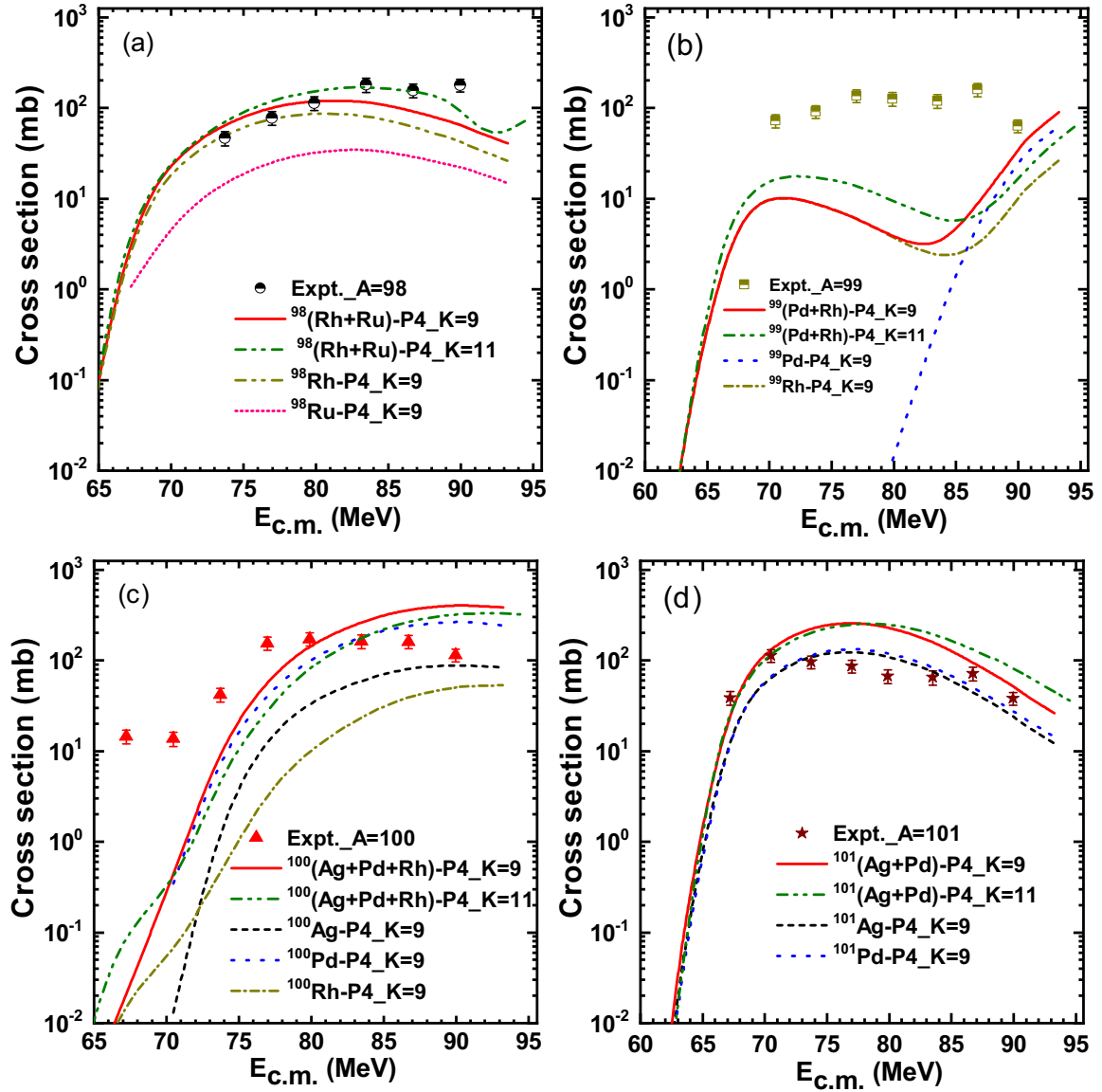


FIG. 5. Comparison between the measured excitation function of different ERs of mass (a) 98 (^{98}Ru and ^{98}Rh), (b) 99 (^{99}Rh + ^{99}Pd), (c) 100 (^{100}Rh + ^{100}Pd + ^{100}Ag), and (d) 101 (^{101}Pd + ^{101}Ag) with PACE4 (denoted P4).

hot and compact fused system. Here, higher fragmentation potential corresponds to lower preformation probability, hence relatively less favorable decay.

Investigation on the fragmentation potential, as shown in Fig. 7(a) for below barrier ($E_{c.m.} = 61.4$ MeV) and Fig. 7(b) for above barrier ($E_{c.m.} = 73.7$ MeV), at the extreme values of angular momentum shows the variation of fragmentation potential with fragment mass number A_2 for the decay of $^{105}\text{Ag}^*$. It suggests that, at l_{\min} , ERs are more probable for addressing the total fusion cross sections. Even though the contribution of IMFs and FFs increases at l_{\max} , yet the effective contribution from all the angular momenta yields larger ER cross sections. The contribution of the decay fragments to the cross section is negligible below l_{\min} . l_{\min} and l_{\max} are decided from the strength of penetrability and preformation probability, respectively. The fragmentation potential term contains

T -dependent liquid drop part of binding energy (V_{LDM}) and shell corrections (δU), and the shell structure effect comes into the picture for $T \leq 1.5$ MeV. Therefore, besides exploring the reaction dynamics related to the $^{37}\text{Cl} + ^{68}\text{Zn}$ reaction, an attempt has been made to explore the shell closure effect of decay fragments. The fragmentation potential curve shows some dips corresponding to $A_2 = 4, 15,$ and 26 for below and above the barrier. The dips for ^4He and ^{15}N are due to deformed shell closure with neutron magic numbers (2 and 8), but the observed dip corresponding to ^{26}Mg , which gets reduced at higher energies as compared with the lower ones, is due to the deformation, as seen in Fig. 7(a) and 7(b). This dip could be due to the inappropriate β_{2i} values, which gets ruled out because of their small penetrability P across the interaction barrier. Figures 7(c) and 7(d) show the variation of preformation probability P_0 calculated at the extreme l

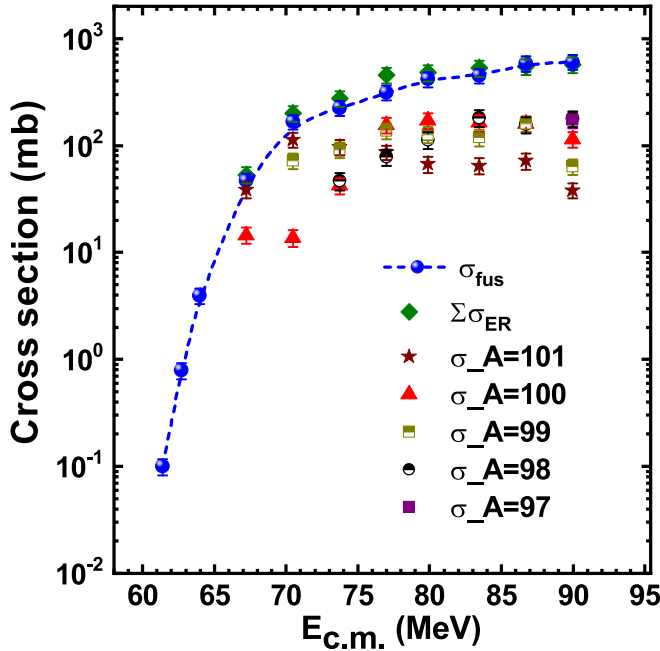


FIG. 6. Experimentally measured fusion cross sections σ_{fus} , sum of the ERs ($\Sigma\sigma_{\text{ER}}$), and cross sections of ERs having masses 97, 98, 99, 100, and 101 u versus $E_{\text{c.m.}}$.

values as a function of A_2 at energies 61.4 and 73.7 MeV for the decay of $^{105}\text{Ag}^*$. The fragment mass distribution obtained from the deexcitation of CN $^{105}\text{Ag}^*$ is symmetric in the two energy regions. It is worth mentioning here that the behavior of P_0 for decaying fragments at below and above barrier energies ensures the dominance of light particles ($1n$, $2n$, ^3H , and ^4He) in comparison with remaining decaying fragments at minimum angular momentum; however, the result gets reversed at higher angular momenta. One can observe the humps for masses corresponding to 4, 15, and 26 in the fragment preformation yield. This observation is consistent

with that obtained earlier from the variation of fragmentation potential. As the temperature effect dominates over the deformation effect, the observed hump for mass 26 gets reduced with increment in energy.

The DCM predicted total ER cross sections at different $E_{\text{c.m.}}$, T , ΔR , and ℓ_{max} are listed in Table I to compare with the measured fusion cross sections of the $^{37}\text{Cl} + ^{68}\text{Zn}$ reaction. It shows a good agreement between the two.

D. Fusion-barrier parameters

Because it is hard to measure the fusion-barrier height and radius directly from the dynamics, one can obtain them indirectly from the measured fusion cross sections. The fusion barrier (V_B) of the $^{37}\text{Cl} + ^{68}\text{Zn}$ reaction has been extracted from the experimentally measured complete fusion cross sections. According to Wong's formula [53], the fusion cross section σ_{fus} can be expressed as a simplified classical formula for energies well above the Coulomb barrier, i.e., $(E_{\text{c.m.}} - V_B) \geq \hbar\omega/2\pi$ as shown in Eq. (4):

$$\sigma_{\text{fus}}(E_{\text{c.m.}}) = \pi R_b^2 \left(1 - \frac{V_B}{E_{\text{c.m.}}}\right), \quad (4)$$

where V_B , R_b , and $\hbar\omega$ are the height, radius, and curvature of the one dimensional barrier, respectively. The measured fusion cross sections σ_{fus} from the $^{37}\text{Cl} + ^{68}\text{Zn}$ reaction show a linear pattern against the inverse of energy ($1/E_{\text{c.m.}}$) following Eq. (4), as presented in Fig. 8. Three below-barrier energy points have been omitted here to obtain the best linear fit through the measured data to obtain the one-dimensional Coulomb barrier parameters. The intercept and slope of the linear fit are the measure of R_b and V_B , respectively. The calculated Bass barrier radius $R_b = r_0(A_p^{1/3} + A_t^{1/3})$ with $r_0 = 1.2$ fm, is 8.9 fm, whereas the DCM estimated barrier radius is 10 fm. The estimated barrier height and radius from the measured cross sections are 65.9 MeV and 8.5 fm, respectively. The predicted barrier height from the Bass model and DCM is 65.5 and 66.6 MeV, respectively, close to the measurement.

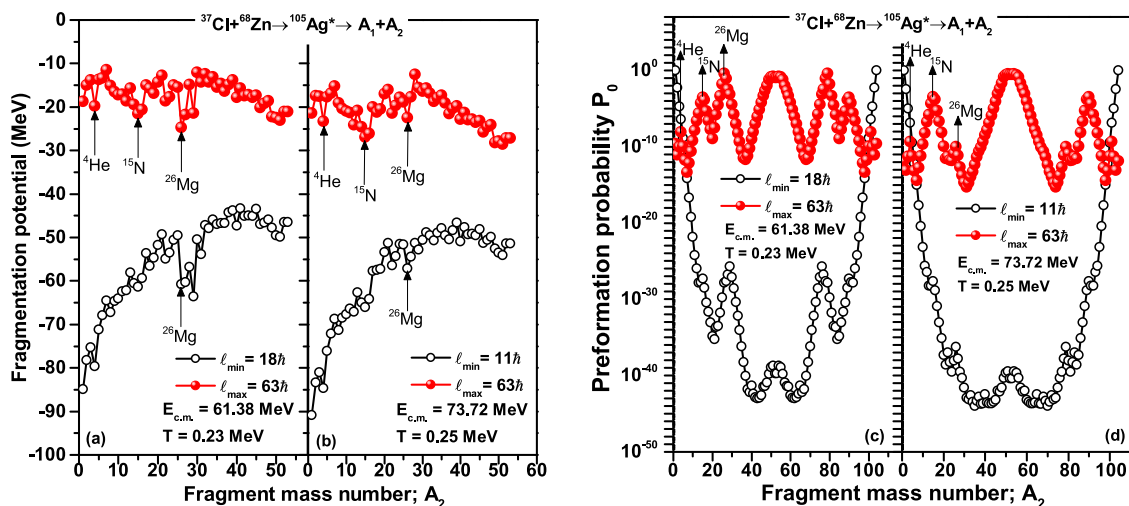


FIG. 7. Fragmentation potential V (MeV) of the CN $^{105}\text{Ag}^*$ formed via the $^{37}\text{Cl} + ^{68}\text{Zn}$ reaction as a function of fragment mass number A_2 at (a) $E_{\text{c.m.}} = 61.4$ and (b) 73.7 MeV. Preformation probability P_0 as a function of A_2 for $^{105}\text{Ag}^*$ at (c) $E_{\text{c.m.}} = 61.4$ and (d) 73.7 MeV.

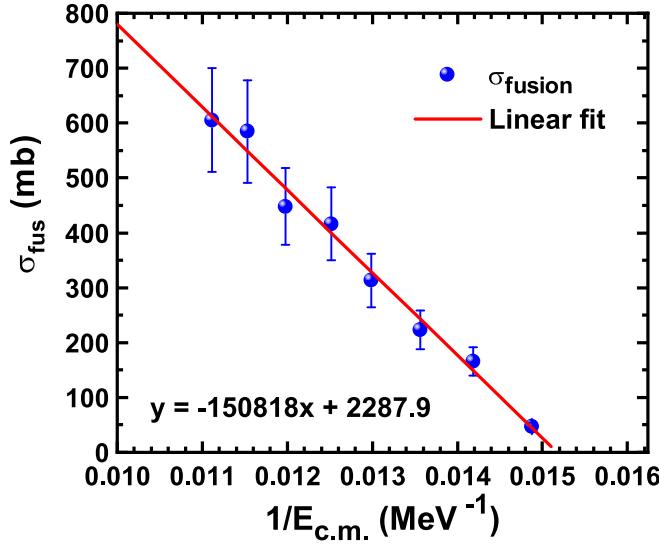


FIG. 8. Variation of total fusion cross sections σ_{fus} of $^{37}\text{Cl} + ^{68}\text{Zn}$ system as a function of energy ($1/E_{\text{c.m.}}$). Solid line is a linear fit through the data.

The measured and theoretical values of V_B and R_b are listed in Table III.

E. Comparison with other ^{37}Cl -induced reactions

To understand the role of the nuclear structure effect on fusion cross sections at near-barrier energies, a few systems such as $^{37}\text{Cl} + ^{24}\text{Mg}$ [54], $^{37}\text{Cl} + ^{59}\text{Co}$ [9], $^{37}\text{Cl} + ^{58,64}\text{Ni}$ [22], $^{37}\text{Cl} + ^{68}\text{Zn}$ (present work), $^{37}\text{Cl} + ^{70,72,73,74,76}\text{Ge}$ [13], and $^{37}\text{Cl} + ^{130}\text{Te}$ [8] have been compared in Fig. 9. The fusion cross sections σ_{fus} and $E_{\text{c.m.}}$ are scaled by the respective maximum geometrical cross section πR^2 and Bass-barrier height V_B , respectively, in this figure. These reduced parameters are adopted to visualize the differences in nuclear radius and barrier position of different systems in order to make a comparison between them [55].

Different properties of the compared systems such as target deformation, fusion nucleus Q value (Q_{fus}), ground-state Q value (Q_{gg}) of the neutron and proton pickup and stripping channels, are given in Tables IV and V. As can be observed from Fig. 9, the measured fusion cross sections for the $^{37}\text{Cl} + ^{68}\text{Zn}$ reaction are slightly lower than for the other systems. This difference could be understood in terms of the nuclear structural properties of different targets. As presented in Table IV, the deformation parameter of ^{24}Mg is two to three times higher than for the other targets, hence the barrier height gets reduced, and fusion probability is enhanced in

TABLE III. Estimated nuclear potential parameters for $^{37}\text{Cl} + ^{68}\text{Zn}$ reaction.

Method	V_B (MeV)	R_b (fm)
Experiment	65.9	8.5
Bass model	65.5	8.89
DCM	66.6	10.0

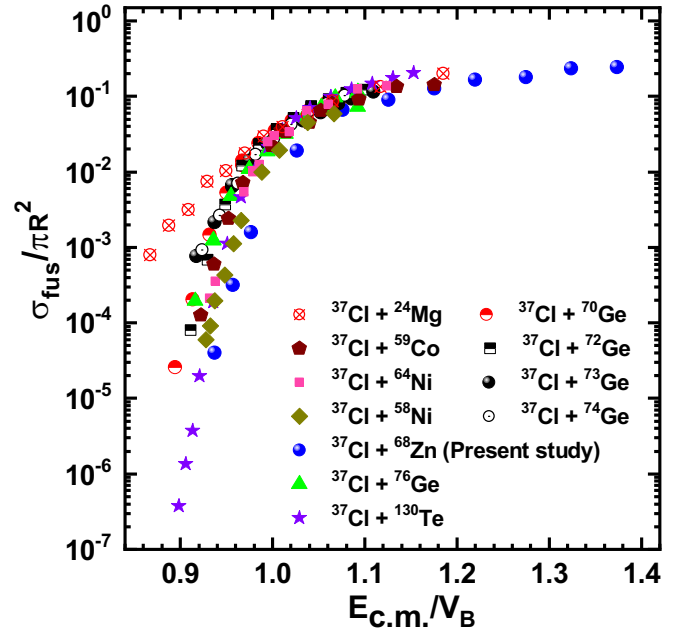


FIG. 9. Reduced fusion excitation functions of ^{37}Cl induced reaction on different targets compared with presently studied system $^{37}\text{Cl} + ^{68}\text{Zn}$. Fusion data for the comparison have been taken from literature as referenced in the text.

$^{37}\text{Cl} + ^{24}\text{Mg}$ system. The σ_{fus} of ^{37}Cl with $^{58,64}\text{Ni}$ and ^{59}Co systems are overlapping in the subbarrier region. However, neutron stripping and proton pickup channels in $^{37}\text{Cl} + ^{58}\text{Ni}$ reactions and proton pickup channels in the $^{37}\text{Cl} + ^{59}\text{Co}$ system may be more effective due to their respective positive Q

TABLE IV. Excitation energies (E^*), spin-parity (J^π), transition (E_λ), and deformation parameters (β_λ) of different targets selected for the comparison as referenced in the text. Fusion Q values (Q_{fus}) of ^{37}Cl in different targets are also listed.

Target nucleus	E^* (MeV)	J^π	E_λ	β_λ	Q_{fus}
^{24}Mg	1.37	2^+	2	0.60	16.29
	7.62	3^-	3	0.32	
^{59}Co	1.072	2^+	2	0.23	-7.91
	4.001	3^-	3	0.19	
^{58}Ni	1.45	2^+	2	0.18	-13.65
	4.47	3^-	3	0.22	
^{64}Ni	1.34	2^+	2	0.17	-11.45
	3.56	3^-	3	0.15	
^{70}Ge	1.04	2^+	2	0.23	-18.76
	2.56	3^-	3	0.23	
^{72}Ge	0.83	2^+	2	0.25	-17.86
	2.51	3^-	3	0.24	
^{73}Ge	0.013	$(5/2)^+$	2	0.24	-16.59
	0.069	$(7/2)^+$	2	0.32	
^{74}Ge	0.60	2^+	2	0.29	-16.79
	2.54	3^-	3	0.16	
^{76}Ge	0.56	2^+	2	0.27	-15.61
	2.69	3^-	3	0.14	
^{130}Te	1.59	2^+	2	0.11	-56.57

TABLE V. The ground-state Q value (Q_{gg}) of neutron and proton pickup and stripping channels (MeV) from $1n$ and $2n$ and $1p$ and $2p$ transfer channels for various projectile-target combinations used for comparison in Fig. 9.

System	+1n	+2n	-1n	-2n	+1p	+2p	-1p	-2p
$^{37}\text{Cl} + ^{24}\text{Mg}$	-10.42	-15.49	-2.98	-0.47	-1.45	-3.86	-6.11	-13.69
$^{37}\text{Cl} + ^{59}\text{Co}$	-4.35	-4.85	-2.82	-2.08	+2.88	-2.7	+1.15	-7.15
$^{37}\text{Cl} + ^{58}\text{Ni}$	-6.11	-8.28	-1.31	+1.49	+2.07	+2.42	-4.97	-12.96
$^{37}\text{Cl} + ^{64}\text{Ni}$	-3.55	-2.31	-4.21	-3.84	-2.29	-6.17	-0.93	-5.10
$^{37}\text{Cl} + ^{70}\text{Ge}$	-5.42	-5.54	-2.89	-0.72	+1.72	+1.49	-3.77	-9.59
$^{37}\text{Cl} + ^{72}\text{Ge}$	-4.64	-3.98	-3.53	-1.91	+0.51	-0.98	-2.73	-7.27
$^{37}\text{Cl} + ^{73}\text{Ge}$	-0.67	-3.35	-0.11	-2.19	0.24	-1.92	-1.53	-6.03
$^{37}\text{Cl} + ^{74}\text{Ge}$	-4.09	-2.79	-3.80	-2.95	-0.77	-3.23	-1.48	-5.07
$^{37}\text{Cl} + ^{76}\text{Ge}$	-3.32	-1.75	-4.24	-4.10	-1.79	-5.41	-0.39	-3.09
$^{37}\text{Cl} + ^{130}\text{Te}$	-2.31	-0.32	-4.38	-4.91	+0.23	-1.94	-1.01	-4.98

values when the excitation energies and deformations are almost the same in all three reactions. The fusion cross sections with all the Ge isotopes are almost similar due to the nearly identical deformation parameters and excitation energies of low-lying excited states except for ^{73}Ge , while those for ^{68}Zn excited states are slightly smaller as compared with the Ge isotopes. It possibly led to a more favorable condition to fuse ^{37}Cl in Ge isotopes compared with ^{68}Zn , which slightly enhanced the subbarrier fusion cross sections in the former cases.

V. CONCLUSION

In the present study, fusion excitation functions have been experimentally measured for the $^{37}\text{Cl} + ^{68}\text{Zn}$ system within the energy range $E_{c.m.} = 61.4\text{--}90.0$ MeV. The measured fusion cross sections have been analyzed within the framework of a coupled-channels calculation and the DCM. The observed enhancement in the subbarrier fusion cross section over the 1d-BPM predictions has been explained by considering the low-lying inelastic excitations among the interacting partners in CCFULL. Additionally, the residual cross sections of several mass fractions (98, 99, 100, and 101 u) have been extracted from the gated spectrum. The measured total fusion cross section σ_{fus} was found approximately equal to the sum of various ER cross sections ($\Sigma\sigma_{\text{ER}}$), although the Hauser-Feshbach model could not reproduce the cross sections of individual residual mass fractions except mass 98 u. Further-

more, deformation and shell effect in the decay of $\text{CN } ^{105}\text{Ag}^*$ has been explored with DCM. The DCM-calculated fusion cross sections are in good agreement with the experimental data. One-dimensional barrier-height and radius parameters extracted from the measured data are in good agreement with the Bass model and the DCM parameters.

ACKNOWLEDGMENTS

We extend our sincere thanks to (i) the IUAC Pelletron group for their cooperation during the experiment, (ii) the IUAC target laboratory team for their help in target preparation, and (iii) the IUAC RBS team for characterization of the target. We also acknowledge the effort of D. Kumar for the fabrication of the ^{68}Zn target during his research tenure at IIT Roorkee. M.M. and G.S. are thankful to the late Professor R.K. Gupta, PU, and Professor M.K. Sharma, TIET, Patiala, India, for their guidance on DCM-analysis. M.M. acknowledges Research Grant No. CRG/2018/002354 from SERB(IN) and Grant No. 03(1467)/19/EMR-II from CSIR(IN). Students' research fellowships from MHRD and DST INSPIRE (IF-180078), Government of India, are also gratefully acknowledged.

The work plan was conceptualized by M.M., A.C., N.M., and S.N. A.C. took the lead in executing the experiment and did preliminary data analysis. R.P. and G.S. participated in the experiment and took the lead in data analysis and paper preparation with M.M. All the authors contributed to the experiment.

- [1] A. B. Balantekin and N. Takigawa, *Rev. Mod. Phys.* **70**, 77 (1998).
- [2] G. Wallerstein, I. Iben, Jr., P. Parker, A. M. Boesgaard, G. M. Hale, A. E. Champagne, C. A. Barnes, F. Käppeler, V. V. Smith, R. D. Hoffman *et al.*, *Rev. Mod. Phys.* **69**, 995 (1997).
- [3] Y. T. Oganessian, A. V. Yeremin, A. G. Popeko, S. L. Bogomolov, G. V. Buklanov, M. L. Chelnokov, V. I. Chepigin, B. N. Gikal, V. A. Gorshkov, G. G. Gulbekian *et al.*, *Nature (London)* **400**, 242 (1999), and references therein.
- [4] B. B. Back, H. Esbensen, C. L. Jiang, and K. E. Rehm, *Rev. Mod. Phys.* **86**, 317 (2014).
- [5] M. Beckerman, *Rep. Prog. Phys.* **51**, 1047 (1988).
- [6] M. Dasgupta, D. J. Hinde, N. Rowley, and A. M. Stefanini, *Annu. Rev. Nucl. Part. Sci.* **48**, 401 (1998).
- [7] J. R. Leigh, M. Dasgupta, D. J. Hinde, J. C. Mein, C. R. Morton, R. C. Lemmon, J. P. Lestone, J. O. Newton, H. Timmers, J. X. Wei *et al.*, *Phys. Rev. C* **52**, 3151 (1995).
- [8] R. N. Sahoo, M. Kaushik, A. Sood, P. Kumar, A. Sharma, S. Thakur, P. P. Singh, P. K. Raina, Md. M. Shaikh, R. Biswas *et al.*, *Phys. Rev. C* **99**, 024607 (2019).
- [9] M. Dasgupta, A. Navin, Y. K. Agarwal, C. V. K. Baba, H. C. Jain, M. L. Jhingan, and A. Roy, *Nucl. Phys. A* **539**, 351 (1992).

- [10] S. Kalkal, S. Mandal, N. Madhavan, E. Prasad, S. Verma, A. Jhingan, R. Sandal, S. Nath, J. Gehlot, B. R. Behera *et al.*, *Phys. Rev. C* **81**, 044610 (2010).
- [11] S. Kalkal, S. Mandal, N. Madhavan, A. Jhingan, E. Prasad, R. Sandal, S. Nath, J. Gehlot, R. Garg, G. Mohanto *et al.*, *Phys. Rev. C* **83**, 054607 (2011).
- [12] Khushboo, S. Mandal, S. Nath, N. Madhavan, J. Gehlot, A. Jhingan, N. Kumar, T. Banerjee, G. Kaur, K. R. Devi *et al.*, *Phys. Rev. C* **96**, 014614 (2017).
- [13] E. Martínez-Quiroz, E. F. Aguilera, J. J. Kolata, and M. Zahar, *Phys. Rev. C* **63**, 054611 (2001).
- [14] V. V. Sargssyan, G. G. Adamian, N. V. Antonenko, W. Scheid, C. J. Lin, and H. Q. Zhang, *Phys. Rev. C* **85**, 037602 (2012).
- [15] R. G. Stokstad, Y. Eisen, S. Kaplanis, D. Pelte, U. Smilansky, and I. Tserruya, *Phys. Rev. Lett.* **41**, 465 (1978).
- [16] J. J. Vega, E. F. Aguilera, G. Murillo, J. J. Kolata, A. Morsad, and X. J. Kong, *Phys. Rev. C* **42**, 947 (1990).
- [17] A. M. Stefanini, L. Corradi, A. M. Vinodkumar, Y. Feng, F. Scarlassara, G. Montagnoli, S. Beghini, and M. Bisogno, *Phys. Rev. C* **62**, 014601 (2000).
- [18] J. C. Mahon, L. L. Lee Jr, J. F. Liang, C. R. Morton, N. T. P. Bateman, K. Yildiz, and B. M. Young, *J. Phys. G* **23**, 1215 (1997).
- [19] H. M. Jia, C. J. Lin, L. Yang, X. X. Xu, N. R. Ma, L. J. Sun, F. Yang, Z. D. Wu, H. Q. Zhang, Z. H. Liu *et al.*, *Phys. Lett. B* **755**, 43 (2016).
- [20] D. O. Kataria, A. K. Sinha, J. J. Das, N. Madhavan, P. Sugathan, L. T. Baby, I. Mazumdar, R. Singh, C. V. K. Baba, Y. K. Agarwal *et al.*, *Phys. Rev. C* **56**, 1902 (1997).
- [21] V. V. Sargssyan, G. G. Adamian, N. V. Antonenko, W. Scheid, and H. Q. Zhang, *Phys. Rev. C* **91**, 014613 (2015).
- [22] S. J. Skorka, A. M. Stefanini, G. Fortuna, R. Pengo, W. Meczynski, G. Montagnoli, A. Tivelli, S. Beghini, C. Signorini, and P. R. Pascholati, *Z. Phys. A: At. Nucl.* **328**, 355 (1987).
- [23] J. O. Newton, C. R. Morton, M. Dasgupta, J. R. Leigh, J. C. Mein, D. J. Hinde, H. Timmers, and K. Hagino, *Phys. Rev. C* **64**, 064608 (2001).
- [24] K. Hagino, N. Rowley, and M. Dasgupta, *Phys. Rev. C* **67**, 054603 (2003).
- [25] J. O. Newton, R. D. Butt, M. Dasgupta, D. J. Hinde, I. I. Gontchar, C. R. Morton, and K. Hagino, *Phys. Rev. C* **70**, 024605 (2004).
- [26] R. Prajapat and M. Maiti, *Phys. Rev. C* **101**, 064620 (2020).
- [27] P. R. S. Gomes, R. Linares, J. Lubian, C. C. Lopes, E. N. Cardozo, B. H. F. Pereira, and I. Padron, *Phys. Rev. C* **84**, 014615 (2011).
- [28] R. Prajapat and M. Maiti, *Phys. Rev. C* **101**, 024608 (2020).
- [29] A. Chauhan and M. Maiti, *Phys. Rev. C* **99**, 034608 (2019).
- [30] D. Kumar, M. Maiti, and S. Lahiri, *Phys. Rev. C* **96**, 014617 (2017).
- [31] D. Kumar and M. Maiti, *Phys. Rev. C* **96**, 044624 (2017).
- [32] R. Prajapat, M. Maiti, D. Kumar, and A. Chauhan, *Phys. Scr.* **95**, 055306 (2020).
- [33] A. Chauhan, M. Maiti, and S. Lahiri, *Phys. Rev. C* **99**, 064609 (2019).
- [34] D. Kumar, M. Maiti, and S. Lahiri, *Phys. Rev. C* **94**, 044603 (2016).
- [35] M. Maiti and S. Lahiri, *Phys. Rev. C* **84**, 067601 (2011).
- [36] M. Maiti and S. Lahiri, *Phys. Rev. C* **81**, 024603 (2010).
- [37] D. Kumar and M. Maiti, *Phys. Rev. C* **95**, 064602 (2017).
- [38] D. Kumar, M. Maiti, and S. Lahiri, *J. Radioanal. Nucl. Chem.* **313**, 655 (2017).
- [39] A. K. Sinha, N. Madhavan, J. J. Das, P. Sugathan, D. O. Kataria, A. P. Patro, and G. K. Mehta, *Nucl. Instrum. Methods Phys. Res., Sect. A* **339**, 543 (1994).
- [40] S. Nath, P. V. Rao, S. Pal, J. Gehlot, E. Prasad, G. Mohanto, S. Kalkal, J. Sadhukhan, P. D. Shidling, K. S. Golda *et al.*, *Phys. Rev. C* **81**, 064601 (2010).
- [41] S. Nath, *Comput. Phys. Commun.* **180**, 2392 (2009).
- [42] A. Gavron, *Phys. Rev. C* **21**, 230 (1980).
- [43] S. Nath, *Nucl. Instrum. Methods Phys. Res., Sect. A* **576**, 403 (2007).
- [44] K. Hagino, N. Rowley, and T. Kruppa, *Comput. Phys. Commun.* **123**, 143 (1999).
- [45] R. Bass, *Nucl. Phys. A* **231**, 45 (1974).
- [46] C. M. Perey and F. G. Perey, *At. Data Nucl. Data Tables* **17**, 1 (1976).
- [47] R. K. Gupta, M. Balasubramaniam, R. Kumar, D. Singh, and C. Beck, *Nucl. Phys. A* **738**, 479 (2004).
- [48] R. K. Gupta, M. K. Sharma, S. Singh, R. Nouicer, and C. Beck, *Phys. Rev. C* **56**, 3242 (1997).
- [49] G. Kaur and M. K. Sharma, *Int. J. Mod. Phys. E* **23**, 1450063 (2014).
- [50] M. K. Sharma, S. Kanwar, G. Sawhney, R. K. Gupta, and W. Greiner, *J. Phys. G* **38**, 055104 (2011).
- [51] R. K. Gupta, M. Balasubramaniam, R. Kumar, D. Singh, C. Beck, and W. Greiner, *Phys. Rev. C* **71**, 014601 (2005).
- [52] P. Möller, J. R. Nix, W. D. Myers, and W. J. Swiatecki, *At. Data Nucl. Data Tables* **59**, 185 (1995).
- [53] C. Y. Wong, *Phys. Rev. Lett.* **31**, 766 (1973).
- [54] S. I. Cavallaro, M. L. Sperduto, B. Delaunay, J. Delaunay, A. D'Onofrio, and H. Dumont, *Nucl. Phys. A* **513**, 174 (1990).
- [55] Z. Kohley, J. F. Liang, D. Shapira, R. L. Varner, C. J. Gross, J. M. Allmond, A. L. Caraley, E. A. Coello, F. Favela, K. Lagergren *et al.*, *Phys. Rev. Lett.* **107**, 202701 (2011).